

PAPER

Water and xenon ECR ion thruster—comparison in global model and experiment

To cite this article: Yuichi Nakagawa *et al* 2020 *Plasma Sources Sci. Technol.* **29** 105003

View the [article online](#) for updates and enhancements.

You may also like

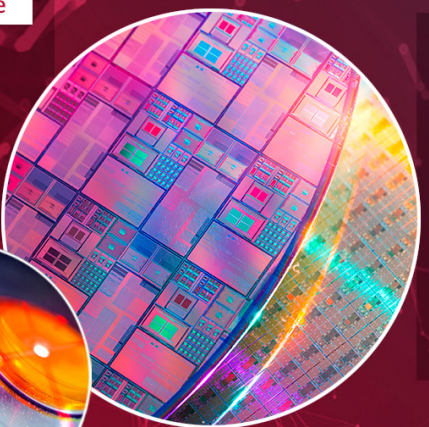
- [Water-filled heat pipes for CubeSat thermal control](#)
H J van Gerner, H Brouwer, Z de Groot et al.
- [Review of in-space plasma diagnostics for studying the Earth's ionosphere](#)
Luis Fernando Velásquez-García, Javier Izquierdo-Reyes and Hyeonseok Kim
- [CubeSat Spatial Expedition: An Overview From Design To Experimental Verification](#)
G Morettini, G Zucca, C Braccesi et al.

HIDEN
ANALYTICAL

Analysis Solutions for your **Plasma Research**

For Surface Science

- Surface Analysis
- SIMS
- 3D depth Profiling
- Nanometre depth resolution



For Plasma Diagnostics

- Plasma characterisation
- Customised systems to suit plasma Configuration
- Mass and energy analysis of plasma ions
- Characterisation of neutrals and radicals



Click to view our product catalogue

■ Knowledge ■ Experience ■ Expertise

Contact Hiden Analytical for further details:

W www.HidenAnalytical.com
E info@hiden.co.uk

Water and xenon ECR ion thruster—comparison in global model and experiment

Yuichi Nakagawa^{1,*}, Hiroyuki Koizumi², Yuki Naito² and
Kimiya Komurasaki¹

¹ Department of Aeronautics and Astronautics, The University of Tokyo, Bunkyo, Tokyo, Japan

² Department of Advanced Energy, The University of Tokyo, Kashiwa, Chiba, Japan

E-mail: y.nakagawa@al.t.u-tokyo.ac.jp

Received 13 February 2020, revised 22 June 2020

Accepted for publication 3 July 2020

Published 15 October 2020



Abstract

Gridded ion thrusters are one of the most commonly used types of electric propulsion, and alternative propellants have been studied for miniature ion thrusters to meet the demand of propulsion systems for micro-/nano-satellites. Water is a candidate as an alternative non-pressurized propellant for a CubeSat thruster. It is consistent with the CubeSat concept of short-term and low-cost development. In this paper, the characteristics of a miniature water ion thruster were compared with those of a xenon one using a global model and experiments. The dependence of the performance on the mass flow rate and the input microwave power was examined, and the effects of dissociation and doubly charged ions were directly measured by a quadrupole mass spectrometer. The estimates on the model were compared against experimental results for both propellants, and the performance of the thruster operating on xenon propellant was compared to the performance operating on water propellant. In the comparison between the estimates and the experimental results, the two differences were discussed: the one between water and xenon and the other from the experimental result in both cases. A performance decrease in the propellant utilization efficiency and the specific impulse cannot be avoided when using water as a propellant in an ion thruster. However, the ion production cost did not increase, and it showed the capability of water ion thruster for CubeSat application taking advantage of safety, low cost, non-pressurized system, and human-friendliness of water when used as a propellant.

Keywords: ion thruster, electric propulsion, CubeSat propulsion, water plasma, water propellant

(Some figures may appear in colour only in the online journal)

Nomenclature

<i>A</i>	Area	<i>I</i> _{sp}	Specific impulse
<i>C</i>	Gas conductance	<i>K</i>	Rate constant
<i>C</i> _i	Ion production cost	<i>L</i>	Length
<i>D</i>	Diameter	<i>M</i>	Mass
<i>F</i>	Thrust	<i>N</i>	Number
<i>I</i>	Current	<i>N</i> _A	Avogadro number
		<i>P</i>	Power
		<i>P</i> _{modified}	Modified absorbed microwave power
		<i>R</i>	Radius, gas constant
		<i>T</i>	Temperature

* Author to whom any correspondence should be addressed.

V	Volume, voltage
Γ	Flux
c_T	Thrust coefficient
e	Elementary charge
e	Electron
$f_{\text{fit}}(x)$	Fitting function
g	Gravitational acceleration
k	Boltzmann constant
\dot{m}	Mass flow rate
m_e	Mass of electron
n	Density
n	Neutral particle
q	Charge
r_{em}	The ratio of the experiment to the model
r_{mc}	Mass-to-charge ratio
v	Velocity
v_B	Bohm velocity
ε	Energy
η_{div}	Efficiency of beam divergence
η_U	Propellant utilization efficiency
λ	Mean free path
σ	Cross-section, variation
ϕ	Electrical potential
$\alpha, \beta, \gamma, \chi, \psi$, and X	Fitting parameters

Subscripts

AG	Accelerating grid
SG	Screen grid
abs	Absorbed
acc	Accumulator
b	Beam
cal	Calibration
dis	Discharge chamber
e	Elementary charge
e	Electron
elas	Elastic scattering
exp	Experiment
in	Input
iz	Ionization
j	Ion
mfr	Mass flow rate
mod	Model
n	Density
n	Neutral particle
p	Plasma
pre	Pressure
prop	Propellant
s	Sheath
w	Wall of the discharge chamber
κ	Index of reaction

1. Introduction

Gridded ion thrusters are one of the most commonly used types of electric propulsion, along with Hall effect thrusters

[1]. They have a higher specific impulse, which represents the impulse per unit mass of propellant, and many flight heritages in deep space exploration [2, 3] and for north–south station keeping of geosynchronous satellites [4]. A gridded ion thruster generates plasma in the discharge chamber of the ion source by feeding the power and the propellant and accelerates the ions of the plasma using two or three grids. The ion beam generates the thrust and the beam is neutralized by the cathode located on the outside of the ion source. As a propellant for a gridded ion thruster, xenon is commonly used because of its low discharge loss, non-toxicity, and high density under high pressure compared with other gases.

Although xenon has become standard as the propellant, one of the disadvantages is its higher cost compared to other gases, and studies of alternative propellants for gridded ion thrusters and Hall effect thrusters have been conducted [5–11]. For example, Kieckhafer estimated that the cost of ground testing for a 500 kW Hall effect thruster with a specific impulse of 2000 s and anode efficiency of 60% was \$6400 per hour just for propellant [6]. Also, many studies on electrodeless thrusters, especially using a magnetic nozzle, have been conducted using alternative propellants because they mainly focus on the high-power range and the cost is an unavoidable issue [12, 13].

Another disadvantage of xenon is its pressurizing system, which becomes especially important for microsatellites and nanosatellites. In particular, the use of CubeSats, satellites composed of one or several 10 cm cubes, has increased significantly and they require a suitable propulsion system [14, 15]. As electric propulsion for CubeSats or nanosatellites, pulsed plasma thrusters (PPTs) and electrospray thrusters have been developed and tested [16–21]. One important advantage is that these propellants are not pressurized but are stored under atmospheric pressure and at room temperature. This reduces the mass and volume of the structure in contrast with Hall thrusters and ion thrusters, which use pressurized xenon as a propellant. Therefore, non-pressurized propellants for Hall thrusters and ion thrusters have been studied for CubeSat application [22–25]. One candidate for the propellant is iodine because of its high density and high efficiency when used in ion thrusters [7, 10, 11]. An iodine ion thruster was developed and scheduled to be launched with the two 6U CubeSats [26, 27]. However, pure iodine has some disadvantages in terms of safety and corrosiveness.

Water is another candidate for an alternative non-pressurized propellant for CubeSat thrusters [28]. It is absolutely safe for human beings, which has a strong advantage as a green propellant, and it was demonstrated by a CubeSat called AQT-D (Aqua Thruster-Demonstrator), which has a water propulsion system, was delivered to the international space station and deployed from it [29]. Its safety and cost-effectiveness are consistent with the concepts of CubeSat: short-term and low-cost development. Several water propulsion systems have been developed, such as resistojet thrusters [29–32], water electrolysis thrusters, water PPTs [33, 34], and a water ion thruster [22]. Among those, ion thrusters have strong potential to deliver a high total impulse. On the other hand, the oxidation is known as a clear disadvantage of using water and is

fatal for hollow cathodes, which are vulnerable to oxidation and mainly used as both ion source and neutralizer for most ion thrusters.

From the viewpoint of preventing oxidation, an electron cyclotron resonance (ECR) ion thruster is one solution in which a water propellant ion thruster is realized. It generates plasma without an electrode in the discharge chamber and also utilizes ECR plasma as a neutralizer with a negatively biased voltage [35–39]. The concept of an ECR water ion thruster was verified by Nakagawa [22] and its thrust was directly measured using a pendulum-type thrust stand [40]. The measured thrust indicated that the effects of the beam divergence and multiply charged ions were comparable with the case of xenon and the dissociation of water molecules would not have a critical impact on thrust. Additionally, the measured thruster performance was lower than in the case of xenon, as expected from the high ionization energy and potential dissociation of water. Nakamura conducted a detailed analysis of this ECR ion thruster using 3D-full-PIC (Particle-In-Cell) numerical calculation and predicted the molecule populations and higher electron temperature in the water plasma [41]. However, the water-plasma model used included a limited number of reactions among a huge number of potential reactions and needed more experimental data for careful validation. Moreover, the calculation could not grasp the overall trend of the thruster due to its high computational cost. An additional experimental comparison with xenon and water and an explanation using a physical model are required to comprehend the behavior of the water ion thruster and to predict the overall trend of the thruster performance.

In this study, we built water- and xenon-plasma global models and conducted experiments to reveal the characteristics of the water ion thruster compared with the xenon one. Firstly, we introduced the global model of the water and xenon plasma and estimated the parameters: the densities and temperatures of the species and the beam current from the ion source. Secondly, the dependence of the performance on the mass flow rate and the input microwave power is reported to confirm the estimation experimentally, and the effects of dissociation and doubly charged ions were directly measured by a quadrupole mass spectrometer. We discuss the difference between the model and the experiments to comprehend the behavior of the water ion thruster in comparison with the xenon one.

2. Global model of the ion source

A global model describes a steady and uniform plasma by solving the conservation equations of the energy, the particles, and the charges. The parameters are the electron temperature, the ion densities, the neutral particle density, and the plasma potential. Such models were constructed for both positive and negative ionized plasma with radio frequency and ECR discharge [42–45] and also for molecular plasma with dissociation [45]. In the field of electric propulsion, they have been used widely for estimation of thruster performance [46–49] and are a suitable way to estimate it when comparing various kinds of propellants. In this section, the global models for

xenon and water plasma are formulated based on the reactions shown in tables 1 and 2.

The model is described by equations (1)–(7) under the assumption that all the heavy particles have the same temperature. Equation (1) is the conservation equations for the energy between the net energy input and the loss, and equation (2) is the conservation equations for the energy of neutral particles:

$$P_{\text{abs}} = \sum_{\kappa} K_{\kappa} n_{\text{n}} n_{\text{e}} V_{\text{p}} \varepsilon_{\kappa} + \sum_j \Gamma_j A_j q_j \phi_{\text{p}} + 2 \Gamma_{\text{e}} A_{\text{e}} k T_{\text{e}}, \quad (1)$$

$$\frac{3}{2} k \Gamma_{\text{n}} (T_{\text{n}} - T_{\text{w}}) = K_{\text{elas}} n_{\text{n}} n_{\text{e}} V_{\text{p}} \frac{3 m_{\text{e}} T_{\text{e}}}{M_{\text{n}}} \quad (2)$$

where κ is from 1 to 23 for water, and from 1 to 4 for xenon. j stands for the type of ion species. The number corresponds to the number of reactions in tables 1 and 2. Equation (3) is the conservation equation for the number of each ion:

$$K_{\text{iz},j} n_{\text{n}} n_{\text{e}} V_{\text{p}} + \sum_{\kappa'} K_{\kappa'} n_{\text{n}} n_{\text{j'}} V_{\text{p}} = \Gamma_j A_{\text{p}} + \sum_{\kappa} K_{\kappa} n_{\text{n}} n_{\text{j}} V_{\text{p}} \quad (3)$$

where κ includes charge transfer reactions of which the ion: j appears on the left-hand side. Also, κ' includes charge transfer reactions of which the ion: j appears in the right-hand side, and j' is the ion which appears on the left-hand side of the reaction. Equations (4) and (5) are the conservation equations for the number of neutral particles. Equation (4) is the case of water, which is shown as

$$\dot{m}_{\text{prop}} = \dot{m}_{\text{n}} + \dot{m}_{\text{H}_2\text{O}^+} + \sum_{\kappa} K_{\kappa} n_{\text{n}} n_{\text{e}} V_{\text{p}} \quad (4)$$

where κ is from 2 to 4, 13 to 15, and 22 to 24. These are the reactions which H_2O are dissociated. Equation (5) is the case of xenon, which is simply shown as

$$\dot{m}_{\text{prop}} = \dot{m}_{\text{n}} + \dot{m}_{\text{Xe}^+} + \dot{m}_{\text{Xe}^{++}}. \quad (5)$$

Equation (6) is the conservation equation for charge:

$$\frac{1}{4} e \bar{v}_{\text{e}} \exp \left\{ -\frac{e(\phi_{\text{p}} - \phi_{\text{s}})}{k T_{\text{e}}} \right\} A_{\text{e}} \sum_j n_{\text{s},j} = \sum_j q_j n_{\text{s},j} v_{\text{B},j} A_j, \quad (6)$$

and equation (7) is a quasi-neutrality equation:

$$n_{\text{e}} = \sum_j \frac{q_j}{e} n_j. \quad (7)$$

For equations (1)–(3), the rate constants are described as a function of the electron energy as:

$$K_{\kappa} = \langle \sigma_{\kappa} v_{\text{e}} \rangle = 4\pi \left(\frac{m_{\text{e}}}{2\pi k T_{\text{e}}} \right)^{\frac{3}{2}} \int_0^{\infty} \sigma_{\kappa}(v_{\text{e}}) v_{\text{e}}^3 \times \exp \left(-\frac{m_{\text{e}} v_{\text{e}}^2}{2 k T_{\text{e}}} \right) dv_{\text{e}} \quad (8)$$

while assuming the Maxwell distribution function for electrons. The reactions included in the models are shown in tables 1 and 2, and these cross-sections are shown in figures 1 and 2. For the water-plasma model, only the reactions related to H_2O are included for simplification. Also, the reactions

Table 1. Reactions in the water-plasma model.

No.	Reaction type	Reaction	ε_k , eV	Rate constant at 5 eV, $m^3 s^{-1}$	Reference
1	Ionization	$H_2O + e^- \rightarrow H_2O^+ + 2e^-$	12.621	1.36×10^{-15}	[50]
2		$H_2O + e^- \rightarrow OH^+ + H + 2e^-$	18.112	4.00×10^{-16}	[50]
3	Dissociative ionization	$H_2O + e^- \rightarrow O^+ + H_2 + 2e^-$	18.116	3.64×10^{-18}	[50]
4		$H_2O + e^- \rightarrow H^+ + OH + 2e^-$	16.95	3.93×10^{-17}	[50]
5		$H_2O + e^- \rightarrow H_2O^*(1^3B_1) + e^-$	7.0	1.47×10^{-16}	[51–53]
6		$H_2O + e^- \rightarrow H_2O^*(1^1B_1) + e^-$	7.4	7.07×10^{-16}	[51, 54, 55]
7		$H_2O + e^- \rightarrow H_2O^*(1^1A_2) + e^-$	9.1	4.99×10^{-17}	[51, 54, 55]
8	Electronic excitation	$H_2O + e^- \rightarrow H_2O^*(1^3A_1) + e^-$	9.3	8.66×10^{-17}	[51, 52, 56]
9		$H_2O + e^- \rightarrow H_2O^*(2^1A_1) + e^-$	9.7	3.30×10^{-16}	[51, 54, 55]
10		$H_2O + e^- \rightarrow H_2O^*(2^1B_1) + e^-$	10.01	6.08×10^{-17}	[51, 54, 55]
11		$H_2O + e^- \rightarrow H_2O^*(3^1A_1) + e^-$	10.16	4.10×10^{-17}	[51, 54, 55]
12		$H_2O + e^- \rightarrow H_2O^*(1^1B_2) + e^-$	11.1	1.46×10^{-17}	[51, 54, 55]
13		$H_2O + e^- \rightarrow OH^*(A) + H + e^-$	9.15	4.55×10^{-16}	[50]
14	Dissociative excitation	$H_2O + e^- \rightarrow OH + H^*(n=2) + e^-$	15.30	8.38×10^{-18}	[50]
15		$H_2O + e^- \rightarrow OH + H^*(n=3) + e^-$	17.19	8.17×10^{-18}	[50]
16	Elastic scattering	$H_2O + e^- \rightarrow H_2O + e^-$	$\frac{3m_e T_e}{M_{H_2O}}$	2.57×10^{-13}	[42, 50]
17		$H_2O(J=0) + e^- \rightarrow H_2O(J=1) + e^-$	4.269×10^{-3}	2.80×10^{-13}	[50]
18	Rotational excitation	$H_2O(J=0) + e^- \rightarrow H_2O(J=2) + e^-$	1.279×10^{-2}	1.45×10^{-14}	[50]
19		$H_2O(J=0) + e^- \rightarrow H_2O(J=3) + e^-$	2.553×10^{-2}	3.37×10^{-15}	[50]
20		$H_2O(000) + e^- \rightarrow H_2O(010) + e^-$	4.534×10^{-1}	2.42×10^{-15}	[50]
21	Vibrational excitation	$H_2O(000) + e^- \rightarrow H_2O(100 + 001) + e^-$	1.980×10^{-1}	4.96×10^{-15}	[50]
22		$H_2O + e^- \rightarrow OH(X) + H + e^-$	5.10	3.32×10^{-15}	[50]
23	Dissociation	$H_2O + e^- \rightarrow O^*(1^1S) + H_2 + e^-$	9.22	8.49×10^{-18}	[50]
24	Dissociative charge transfer	$H_2O + H_2O^+ \rightarrow H_3O^+ + OH$	—	1.7×10^{-15}	[57]
25		$H_2O + OH^+ \rightarrow H_2O^+ + OH$	—	3.0×10^{-15}	[57]
26	Charge transfer	$H_2O + H^+ \rightarrow H_2O^+ + H$	—	3.0×10^{-15}	[57]
27		$H_2O + O^+ \rightarrow H_2O^+ + O$	—	2.33×10^{-15}	[57]

^aRate constants were calculated from the cross-section and the electron temperature.

^bEmission cross-section was used as an excitation cross-section. It ignored the higher excited states.

^cCharge-transfer cross-section does not depend on the electron temperature.

Table 2. Reactions in the xenon-plasma model.

No.	Reaction	ε_k , eV	Rate constant at 5 eV, $m^3 s^{-1}$	Reference	
1	$Xe + e^- \rightarrow Xe^+ + 2e^-$	12.13	8.42×10^{-15}	[58, 59]	
2	Ionization	$Xe + e^- \rightarrow Xe^{++} + 3e^-$	2.88×10^{-17}	[58, 59]	
3	Electronic excitation	$Xe + e^- \rightarrow Xe^* + e^-$	9.686 eV^a	1.31×10^{-14}	[60]
4	Elastic scattering	$Xe + e^- \rightarrow Xe + e^-$	$\frac{3m_e T_e}{M_{Xe}}$	2.57×10^{-13}	[45, 61]
5	Charge transfer	$Xe^+ + Xe \rightarrow Xe^+ + Xe$	—	3.0×10^{-16}	[62]

^aEstimated by the author from reference [61].

^bCharge-transfer cross-section does not depend on the electron temperature but the ion temperature.

whose rate constants are less than $1.0 \times 10^{-16} m^3 s^{-1}$ for 0 to 20 eV of the electron temperature are not used. The data include the uncertainties in both the cross-sections and the electron energy. For instance, the uncertainties of the ionization cross-sections of H_2O^+ , OH^+ , O^+ , and H^+ are 6%, 7%, 9%, and 6.5%, and that in the electron energy is ± 1 eV [63].

For equations (1) and (3), the fluxes of ions are expressed as:

$$\Gamma_j = n_{s,j} v_{B,j}. \quad (9)$$

For equations (4) and (5), the mass flow rate of the neutral particle is described as:

$$\dot{m}_n = \frac{N_{AG} D_{AG}}{16} \sqrt{\frac{8\pi k T_n}{M_n}} \left[1 + \frac{3}{4} \left\{ \frac{L_{AG}}{D_{AG}} \left(1 + \frac{1}{3 + \frac{6}{7} \frac{L_{AG}}{D_{AG}}} \right) \right\} \right]^{-1} M_n n_n \quad (10)$$

by Santeler's equation [65] while assuming that the mass flow rate of the neutral particle is determined by the conductance of the accelerating grid and the neutral particle density. For the water-plasma model, only H_2O is included as a neutral particle.

Here the cylindrical shape of the plasma is assumed, which has L_p as a height of the plasma and R_p as a radius of the

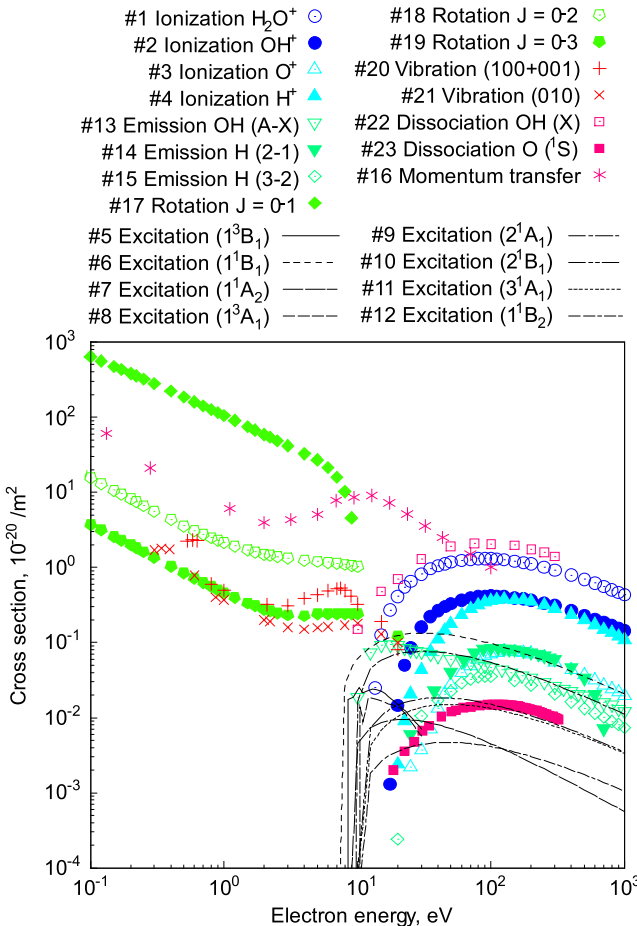


Figure 1. Cross-sections for water-plasma model. Plotted points are based on reference [50]. Excitation cross-sections except for 1^3B_1 and 1^3A_1 are estimated from BE-scaled Born cross-section [54, 64] from generalized oscillator strength in reference [55]. Cross-sections for 1^3B_1 and 1^3A_1 are based on reference [52] and scaled using the experimental data at 20 eV of the electron impact energy in references [53, 56].

plasma, and the ion density at the sheath edge is regarded to be calculated based on reference [42]. The mass flow rates of ions are expressed as:

$$\dot{m}_{j,\text{SG}} = 0.86 \left(3 + \frac{L_p}{2\lambda_j} \right)^{-\frac{1}{2}} M_j n_j v_{\text{B},j} A_{\text{SG}} \quad (11)$$

while neglecting the effect of sheath expansion near the screen grid and the distribution of the plasma. The screen grid current in the model is expressed as:

$$I_{\text{SG}} = \sum_j \frac{q_j \dot{m}_j}{M_j}. \quad (12)$$

For equations (5) and (7), the ion density at the sheath edge is shown as:

$$n_{s,j} = \frac{n_j}{L_p + R_p} \quad (13)$$

$$\left\{ 0.8 L_p \left(4 + \frac{R_p}{\lambda_j} \right)^{-\frac{1}{2}} + 0.86 R_p \left(3 + \frac{L_p}{2\lambda_j} \right)^{-\frac{1}{2}} \right\}$$

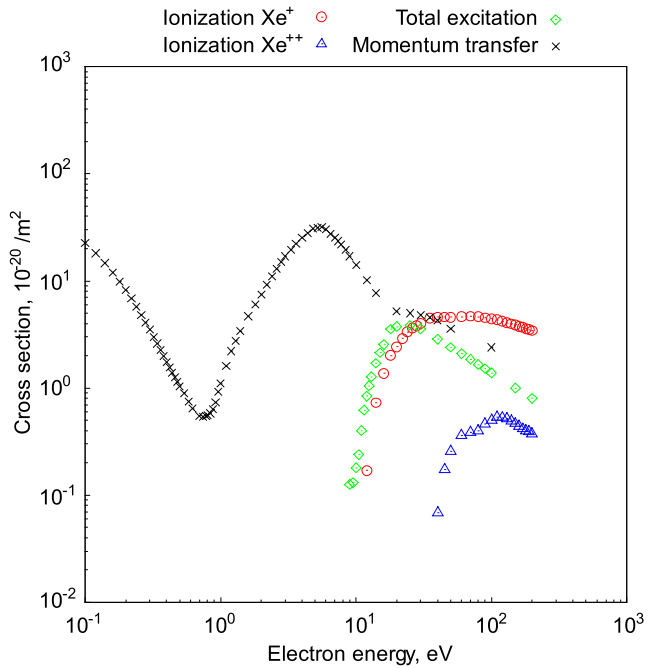


Figure 2. Cross-sections for xenon plasma model [59–61].

where λ_j is the mean free path of ion from reference [42], and here it is led from the charge-transfer cross-section.

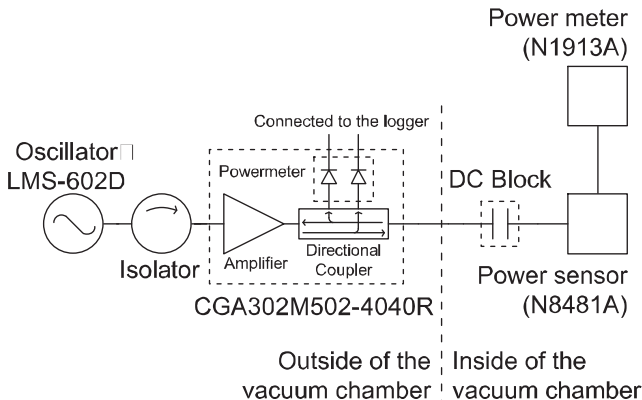
In both the water- and xenon-plasma model, the discharge chamber was assumed to be cylindrical with a diameter of 2.0 cm and a length of 2.0 mm. The loss area of ions is regarded as this cylindrical wall and that of electrons is the two ring-shaped magnets, whose total area of the surface is $1.26 \times 10^{-4} \text{ m}^2$. The diameter of the holes of the screen grid and the accelerating grid are 0.8 mm and 0.4 mm, and the thicknesses of these grids are 0.2 mm and 0.4 mm, and the grids have 289 holes. The temperature of the wall is set at 295 K. The temperature of the plate on which the thruster was mounted was around room temperature in the operation, and here we assumed that the temperature of the wall was 295 K based on this result.

3. Experimental setups

Two kinds of experiments were conducted in this study: the ion source operation for the comparison with xenon and the ion population measurement in the plasma by quadrupole mass spectrometer. In both experiments, the same vacuum system, ion source, microwave power source, and propellant feeding system were used. The DC voltage supplies were only used for the ion source operation experiment because this was the only experiment accelerating the ions.

3.1. Vacuum system

All experiments were conducted in a cylindrical vacuum chamber with a diameter of 1.0 m and a length of 1.2 m. The chamber was pumped by a turbomolecular pump with a pumping speed of 860 l s^{-1} (N2): TG900M produced by Osaka Vacuum Ltd. The back pump of the turbomolecular pump was a rotary pump with oil, which is GHP-1300



*Calibration was conducted in atmospheric pressure

*Components were connected by co-axial cable

Figure 3. Microwave feeding system with calibration test.

produced by DIAVAC Ltd. The pressure of the vacuum chamber was measured by a pressure sensor combined with a Pirani gauge and cold cathode. The measured pressure was less than 5.0×10^{-2} Pa during all experiments. It was higher than that of the typical experiment of the ion thruster, but the backflow and the charge exchanged ions which were caused by the higher pressure do not affect the results in the beam current measurement of the ion source. The pressure of the discharge chamber was sufficiently higher than that of the vacuum chamber, and the charge-exchanged ions do not affect the beam-current measurement in short-time operation. On the other hand, it would affect the measurement by a quadrupole mass spectrometer, and it is discussed in section 5.4.

3.2. Ion source

The ECR ion source had a cylindrical discharge chamber with a diameter of 2.0 cm and a length of 3.0 mm. It had two ring-shaped magnets, an antenna for the microwave, and a screen grid and an accelerating grid to extract the ion beam. The length was defined as the distance from the surface of the magnet to the upstream of the screen grid. The design was based on the xenon ion thruster used in two spacecraft operated in space, and the details of the design can be seen in references [36–38].

3.3. Power sources

A microwave power source and DC voltage power sources were used. The microwave power source consisted of an oscillator (LMS-602D produced by Vauinx Technology Corporation), an isolator, and a unit of an amplifier (CGA302M502-4040R produced by R & K Company Ltd.). The oscillator inputted a signal of 4.25 GHz and 0 dBm to the amplifier, which amplified the signal and inputted the microwave into the ion source through a coaxial cable. A directional coupler with a power sensor was inserted in the path to the ion source and it detected the microwave power supplied to the ion source and the microwave reflected from the ion source using the power sensor. A DC block was also inserted in the path, which prevented a high voltage from being applied to

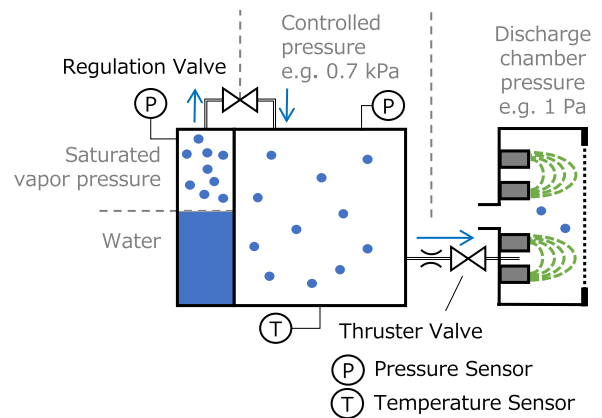


Figure 4. Schematic of propellant feeding system for water.

the microwave power source. The calibration of the microwave power source was conducted with the setup shown in figure 3. The power was changed by modifying the output from the amplifier and was measured by the power sensor (N8481A produced by Agilent technologies) and the power meter (N1913A produced by Agilent technologies). It included the loss of the coaxial cable and the DC block.

The two DC power sources were used. One was HJPR-1.5P40 produced by Matsusada Precision, which could apply 0 to 1.5 kV to the screen grid. The other was PLE-650-0.1 produced by Matsusada Precision, which could apply –650 to 0 V to the accelerating grid. The applied voltages and the currents were measured and the errors were defined by the standard deviation in each period of experiments.

3.4. Propellant feeding system

The propellant feeding system depends on which propellant is used, xenon or water. Xenon was fed from the outside of the vacuum chamber, and the mass flow was controlled by the mass flow controller, which was MS-series mass flow controller whose full range was $44.7 \mu\text{g s}^{-1}$ (0.5 sccm) produced by Alicat scientific. The accuracy of the mass flow controller was the sum of 0.8% of the reading value and 0.2% of its full scale.

The water feeding system was operated in the vacuum chamber. A schematic of the water feeding system is shown in figure 4. The pressure sensors were piezoelectric sensors, which were HSCDANT010KDA5 produced by Honeywell, and the temperature sensors were type K thermocouples. The accuracy of the pressure sensor was 0.25% of full scale. The liquid and the vapor were separated by gravity in the tank, and only the vapor was introduced to the accumulator. The pressure of the accumulator was kept at a certain value by bang–bang control of the regulation valve, and the mass flow was determined by the pressure. The range of the pressure variation was typically 5% of the pressure, which affected the variation of the mass flow rate. The mass flow rate of the vapor was calculated from the pressure in the calibration test. The method used in the calibration test was as below.

- (a). Set the pressure of the accumulator to around 3 kPa with all valves closed.

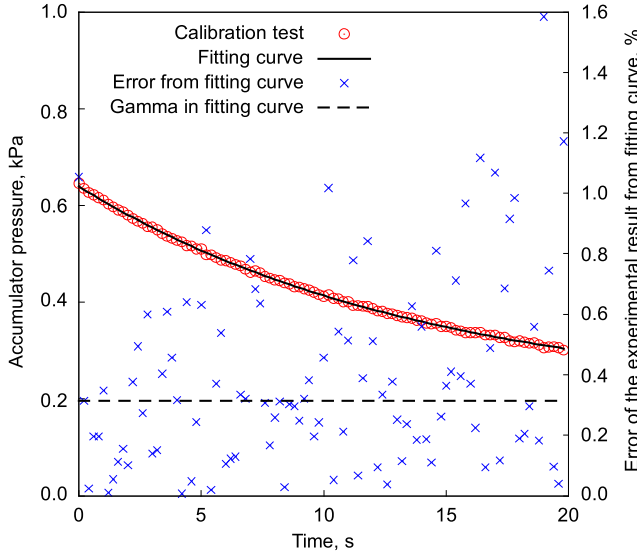


Figure 5. Typical result of the calibration test. Error indicates the difference of the experimental results from the fitting curve.

- (b). Open the thruster valve.
- (c). Wait until the pressure decreases to around 0 kPa.
- (d). Repeat the above steps five times.

Five sets of data were obtained through the procedure, and every data set showed how much the pressure in the accumulator dropped when the vapor was fed to the ion source without the tank feeding any vapor. The typical result of the calibration test is shown in figure 5. The relation between the mass flow rate and the pressure of the accumulator P_{acc} in the test are described by equation (14) under assumptions that the vapor acts as an ideal gas and that the temperature is constant.

$$\dot{m}_n = \frac{M_n N_A V}{RT_n} \dot{P}_{\text{acc}}. \quad (14)$$

The operating pressure of the accumulator was 0.5–1.0 kPa, and the smallest diameter of the path from the accumulator to the discharge chamber was 0.8 mm. The Knudsen number was about 0.5, hence the flow was not regarded as a molecular flow as well as viscous flow. In the case of the molecular flow and the choked flow, the relation between the mass flow rate and the pressure of the accumulator is described using the pressure of the accumulator and the discharge chamber as expressed as:

$$\dot{m}_n = C(P_{\text{acc}} - P_{\text{dis}}) \approx CP_{\text{acc}}. \quad (15)$$

the pressure of the accumulator was of the order of 1 kPa and that of the discharge chamber was 1 Pa, thus the pressure of the discharge chamber could be ignored here. From equations (14) and (15), the pressure of the accumulator should be described as:

$$P_{\text{acc}} = \alpha \exp(\beta t - \chi) + \gamma. \quad (16)$$

As a result, the mass flow rate is described as:

$$\dot{m}_n = \frac{M_n N_A V}{RT_n} \beta (P_{\text{acc}} - \gamma). \quad (17)$$

α, β, γ , and χ were determined from each data set of the calibration test by the least-squares method. The fitting curve was shown in figure 5 with the measured pressure. The errors of the experimental result from the fitting curve were less than 1.6%, and almost all of them were less than 1.0%. It shows that the pressure followed this relation.

In the operation, the pressure of the accumulator was kept at a certain value. The mass flow rate of vapor under a certain experimental condition was expressed using the averaged pressure of the condition with equation (17). The error of the mass flow rate from the calibration, σ_{cal} , was evaluated for n calibration tests using equation (18):

$$\sigma_{\text{cal}} = \frac{M_n N_A V_{\text{acc}}}{RT_n} \sqrt{\frac{1}{n-1} \sum_l^n \{ (\beta_l - \bar{\beta}) P_{\text{acc}} - (\beta_l \gamma_l - \bar{\beta} \bar{\gamma}) \}^2}. \quad (18)$$

The mass flow also varied with the pressure of the accumulator, σ_{pre} , as follows:

$$\sigma_{\text{pre}} = \frac{M N_A V_{\text{acc}}}{RT_n} \bar{\beta} \sqrt{\frac{1}{n-1} \sum_k^n (P_{\text{acc}} - \bar{P}_{\text{acc}})^2}. \quad (19)$$

From these two variations, the variation of the mass flow rate, σ_{mfr} , was defined as:

$$\sigma_{\text{mfr}} = \sqrt{\sigma_{\text{cal}}^2 + \sigma_{\text{pre}}^2}. \quad (20)$$

3.5. Quadrupole mass spectrometer

The quadrupole mass spectrometer (RGA200 produced by stanford research systems) was used for measuring the relative abundance of the ions. It was made of stainless steel with a length of 4.5 inches and a diameter of 0.25 inches. The detector was a Faraday cup. It measured the density of ions as currents for each mass-to-charge ratio. The measurable mass range was 1–200 amu and the resolution was better than 0.5 amu. Data values below 1.5 amu were not used because of the ‘zero blast’ effect [66], which is a common phenomenon in a quadrupole mass spectrometer, and H^+ was out of the measurement range. The acquired absolute value of the mass-to-charge ratio had a maximum error of 0.3–0.5 amu, and it affected the fitting curve in the result section. The measured value had a unit of Torr in the experiment, and it included the effect of the transmission of a quadrupole mass spectrometer. The operational pressure range was less than 1.3×10^{-2} Pa. The spectrometer had a filament to ionize the gas because it was originally for analyzing the mass proportion of the neutral gas. The filament was not heated in the experiment, and the ions from the ion source were directly measured.

3.6. Experimental conditions

In the ion source operation for the performance comparison, the screen voltage and the accelerating voltage were fixed as 1.50 kV and -2.0×10^2 V. The microwave power to the ion source was changed discretely in the range from 0.25 to 6.6 W. The mass flow rate was also changed discretely. Its range was

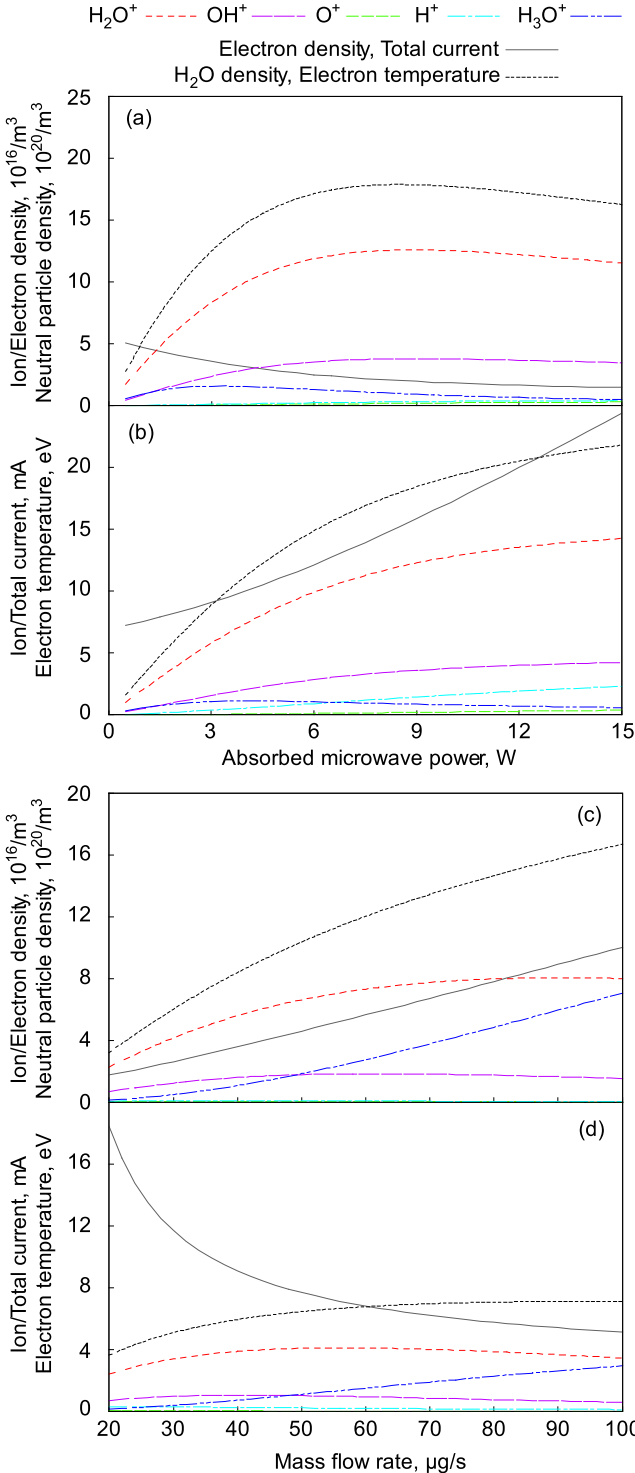


Figure 6. (a) and (b) Water-plasma model at a mass flow rate of $45 \mu g s^{-1}$ while changing absorbed microwave power. (c) and (d) Water-plasma model at absorbed microwave power of 2 W while changing mass flow rate from 20 to $100 \mu g s^{-1}$.

$33.3 \pm 2.0 \mu g s^{-1}$ to $71.2 \pm 3.5 \mu g s^{-1}$ in the case of water and $19.2 \pm 0.24 \mu g s^{-1}$ to $44.8 \pm 0.45 \mu g s^{-1}$ in the case of xenon. The experiments were conducted while changing these two parameters independently. When the plasma could not keep in a certain condition, the data were not shown in the results. An experiment under a certain condition was at least 20 s long,

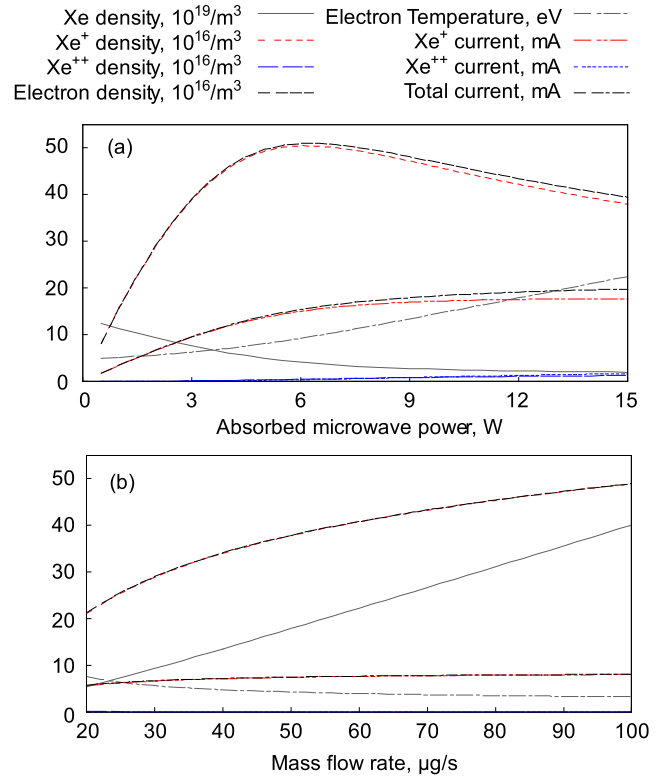


Figure 7. (a) Xenon-plasma model at a mass flow rate of $30 \mu g s^{-1}$ while changing absorbed microwave power. (b) Xenon-plasma model at absorbed microwave power of 2 W while changing mass flow rate from 20 to $100 \mu g s^{-1}$.

and the plots were averaged from the results of several experiments under the same condition. Every experiment under the same condition had a different error, and the maximum error among them was used as the error of the condition.

Measurements of the relative abundance of the ions by the quadrupole mass spectrometer were conducted five times per condition and the measured values were averaged. The ions in the plasma were not accelerated to remove the effect of transparency among the ions. The ion source was located 7 cm from the inlet of the spectrometer and about 18 cm from the Faraday cup. The vacuum chamber pressure met the criterion for operational pressure among the conditions in this paper.

4. Results

4.1. Global model estimation

The results of estimation from the water- and xenon-plasma model while changing the absorbed microwave power are shown in figures 6 and 7. In the water-plasma model, the dominant ion was H_2O^+ . The second highest densities were that of OH^+ for higher absorbed microwave power (figure 6(a)) and that of H_3O^+ for higher mass flow rate (figure 6(c)). Especially the H_3O^+ density increased to almost the same value as that of H_2O^+ because of an increase in neutral density and charge transfer. The other species had densities below 2% of that of H_2O^+ . The screen current in the model was also mainly composed of H_2O^+ , OH^+ , and H_3O^+ current. The H^+ current was

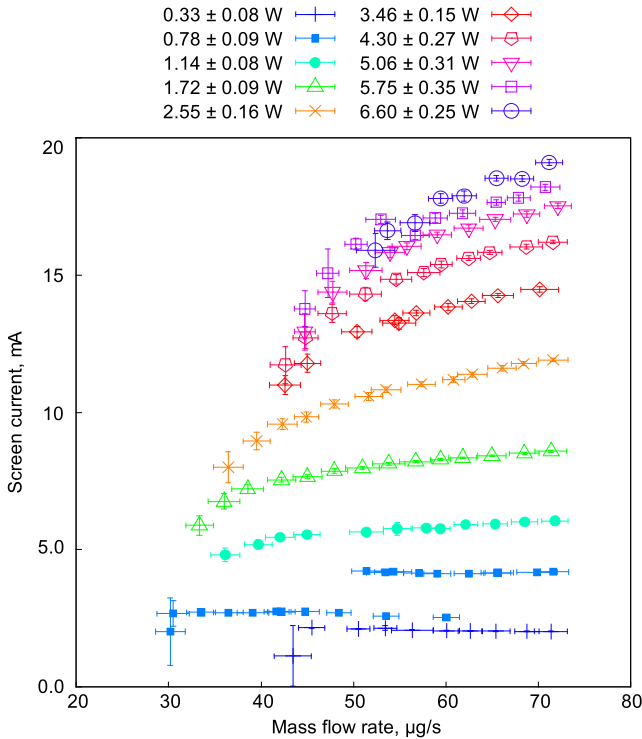
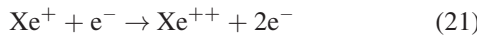


Figure 8. Experimental result of ion source operation: mass flow rate versus screen current when using water. The legends represent the microwave power input.

high relative to its density because of its high Bohm velocity due to the lighter mass of the ion. In figure 7, the result of the xenon-plasma model is shown. The dominant ion was Xe^+ in the xenon-plasma model, as expected. However, the reaction that



was not included in the model, and the Xe^{++} would be underestimated.

On comparing water and xenon, the water required higher mass flow rate than xenon to moderate the increase of the current, and therefore the ideal operating point of a water ion thruster is expected to have a higher mass flow rate than that of a xenon one if the discharge chambers are similar. The current operating range was less than 2 W of microwave power, and under such condition, the current was almost the same, which suggested that the thrust achieved with water dropped to around 40% of that achieved with xenon.

4.2. Ion source operation using water and xenon

The results of the ion source operation using water and xenon are shown in figures 8 and 9. These are thinning-out results, thus the results for certain microwave power inputs are not shown. The current monotonically increased with the power except for over 5.75 ± 0.35 W for water. In this case, the current was almost saturated and the current does not increase significantly. Also, the increment gradually decreased with the power in both water and xenon. The current when using water differed by about 10% from that when using xenon at a similar mass flow rate.

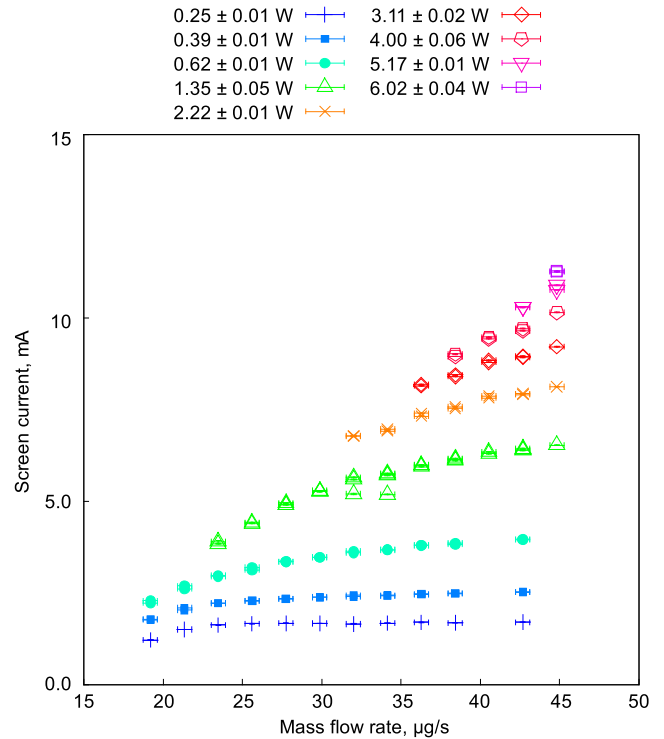


Figure 9. Experimental result of ion source operation: mass flow rate versus screen current when using xenon. The legends represent the microwave power input.

The dependence on the mass flow rate was more moderate than that on the microwave power. In the case of water, the increases of the screen current were less than 20% for a mass flow rate of more than $50 \mu\text{g s}^{-1}$. The curve at the microwave power of 0.78 ± 0.09 W was divided into two parts by the discontinuous point around $50 \mu\text{g s}^{-1}$, and one was almost the same as the value at the power of 0.33 ± 0.08 W. This would be caused by a mode transition of the microwave discharge. Although saturation was also observed in the case of xenon, the split of the curve was not. Another important point was the lower limit of the mass flow rate. On increasing the microwave power, the operating range of the mass flow rate became narrow, and this phenomenon was the same for both water and xenon.

4.3. Measurement of the relative abundance of ions by quadrupole mass spectrometer

The intensity of each mass-to-charge ratio is shown in figure 10(a) for water and figure 11(a) for xenon. In the case of water, the intensity had a strong peak at 18 of mass to charge ratio, corresponding to H_2O^+ , and some weak peaks around it. These weak peaks were the ions made by the dissociative ionizations and the charge transfers, such as OH^+ , O^+ , and H_3O^+ . In figure 11(a), the peaks were only observed around Xe^+ and Xe^{++} . In figures 10(b) and 11(b), the fitting functions of the results are shown. The fitting functions were a superposition of Gaussian functions for the peaks with some offsets to correct the error of the ultimate value of the mass-to-charge ratio r_{mc}

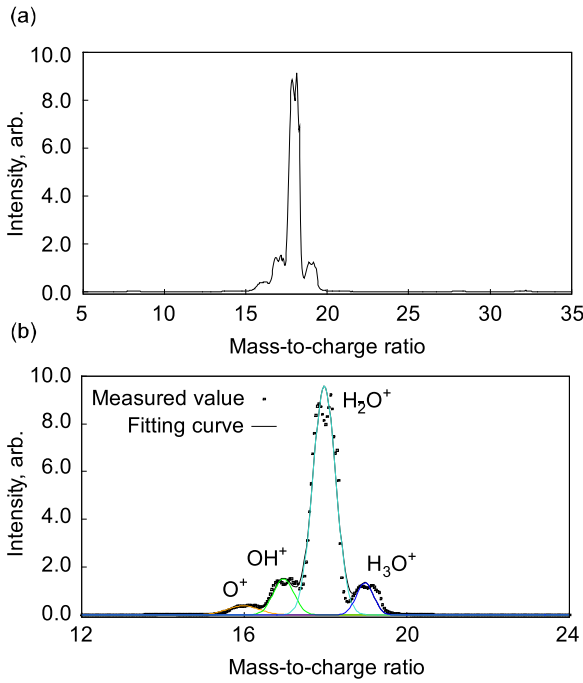


Figure 10. (a) Measured spectrum with the mass-to-charge ratio of water plasma at a microwave power of 2.0 W and mass flow rate of $40 \mu\text{g s}^{-1}$. (b) Fitting functions of the spectrum.

from the quadrupole mass spectrometer using equation (22):

$$f_{\text{fit}}(r_{\text{mc}}) = \sum_j \frac{X_j}{\sqrt{2\pi\sigma_j^2}} \exp \left[-\frac{\{(r_{\text{mc}} + \psi) - r_{\text{mc},j}\}^2}{2\sigma_j^2} \right] - (\alpha_j r_{\text{mc}} + \beta_j). \quad (22)$$

X_j , σ_j , α_j , β_j , and ψ were determined by the least-squares method with the experimental data. The ratio of the species was calculated as the ratio of the integral of each Gaussian function using equation (23):

$$\begin{aligned} \Gamma_{\text{H}_2\text{O}^+} : \Gamma_{\text{OH}^+} : \Gamma_{\text{H}_3\text{O}^+} : \Gamma_{\text{O}^+} \\ = X_{\text{H}_2\text{O}^+} : X_{\text{OH}^+} : X_{\text{H}_3\text{O}^+} : X_{\text{O}^+}. \end{aligned} \quad (23)$$

For example, under the condition shown in figure 10, $\Gamma_{\text{H}_2\text{O}^+} : \Gamma_{\text{OH}^+} : \Gamma_{\text{H}_3\text{O}^+} : \Gamma_{\text{O}^+} = 75.8 : 11.3 : 9.2 : 3.6$.

In the case of xenon, two bunches of peaks existed, corresponding to Xe^+ and Xe^{++} , and each bunch included some fine peaks. They were caused by the stable isotopes of xenon. In table 3, the natural abundance of the isotopes and the measured ratios are compared.

5. Discussion

5.1. Possible differences caused by the assumptions and errors on the global model

Many assumptions and errors were included in the global model as mentioned in section 2. Although the uniformity and Maxwell distribution for the electron were common assumptions on global models, they do not meet the condition of the

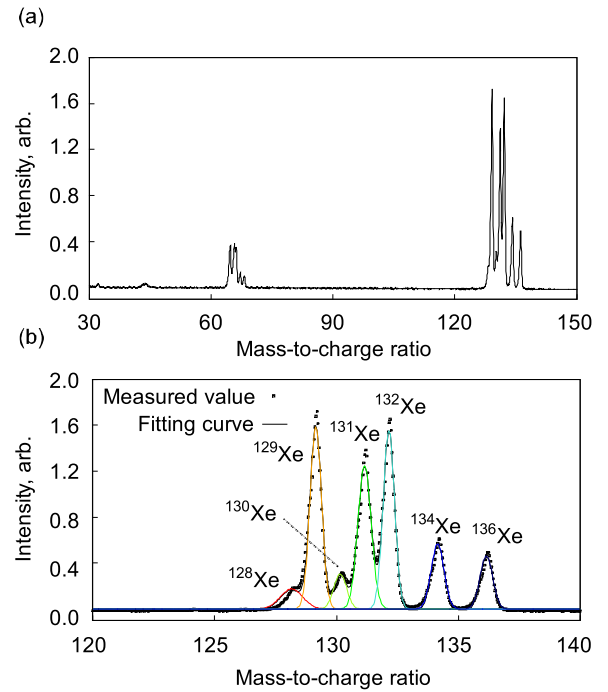


Figure 11. (a) Measured spectrum with the mass-to-charge ratio of xenon plasma at a microwave power of 1.5 W and mass flow rate of $30 \mu\text{g s}^{-1}$. (b) Fitting functions of the spectrum.

Table 3. Natural abundance and measured relative abundance of xenon isotopes.

	Natural abundance [67]	Measured relative abundance
^{124}Xe	0.095(5)%	0.080%
^{126}Xe	0.089(3)%	0.087%
^{128}Xe	1.910(13)%	4.0%
^{129}Xe	26.401(138)%	25.8%
^{130}Xe	4.071(22)%	5.2%
^{131}Xe	21.232(51)%	21.9%
^{132}Xe	26.909(55)%	25.2%
^{134}Xe	10.436(35)%	9.7%
^{136}Xe	8.857(72)%	7.9%

ion source examined in this paper. Also, the gas conductance and the temperature for the neutral particle had differences from the experimental model. The assumption on the reactions and the errors of the cross-sections were especially important for using water. Here, possible differences caused by these assumptions and errors on the global model were discussed.

A big assumption was uniformity, which was one of the most fundamental ones in a global model. Especially since the ion source used ECR heating by the microwave from an antenna, the distribution of the plasma should have a large non-uniformity. This was shown by the 3D-PIC numerical simulation in the cases of both xenon [68] and water [41, 69] and should be one cause of the gap. In addition, the extraction of the beam from the non-uniform plasma was also simulated and non-uniformity would affect the extraction [70].

Another important assumption was a Maxwell distribution for the electron. Although there was no experimental result of

measuring the electron energy distribution function (EEDF) for the ion source and another plasma source as the same size and power as the ion source, some experiments were conducted for ECR plasma source in a different power range [71–73]. They reported the electron distribution had almost two temperatures, which have the lower energy and the higher energy, around the ECR region. It suggested that the assumption of Maxwell distribution be also broken in the ion source, and the EEDF measurement of the ion source was required for further discussion.

The neutral particle density also had errors from the assumption on the gas conductance and its temperature. The gas conductance of the screen grid was only 6.2 times larger than that of the accelerating grid. Although it would not be regarded as the conductance in the pure series because the space between the screen and accelerating grids were so narrow that the velocity of the particle was not random, the screen gird caused the underestimation of the neutral particle density by at least several percent. On the other hand, the temperature would be estimated to be lower than the actual value. The wall temperature was not measured directly and it was regarded the same temperature as that of the plate on which the ion source mounted as mentioned in section 2. It would cause the overestimation of the density of the neutral particle.

Missing species and reactions for simplification would also cause the gap. The neutral particles such as OH, O, and H was ignored in the global model. These were the source of OH⁺, O⁺, and H⁺, and they also have some charge-transfer cross-section with the ions. The amount of the particles cannot be neglected, for example, as OH should be over 10% of H₂O in some condition although it is difficult to include it into the model practically because of the lack of the cross-sections. Also, the data of the cross-sections for water molecules was not completed especially for excitation and dissociation, and it included several important reactions such as dissociation into O(³P) [50]. In addition, the uncertainties included in the data of the cross-section affects the results. For instance, when the model is calculated with six percent larger or smaller ionization cross-section of H₂O⁺ than the used ones, the electron density changes 4%, and when the model is calculated the data with 1 eV larger or smaller electron energy, the electron density changes 5%. It suggests that the uncertainties affect the result by several percent. These reactions were neglected here. Including these species and reactions would help the model be more accurate.

The extraction of ions would also affect the model. The sheath expansion was not included and it affected the net current of ions. Also, the ratio of the ions would be changed because of the difference in Bohm velocities, and it would change the plasma parameters at the same input parameters.

5.2. Comparison of water and xenon based on experiment

From the perspective of the performance as a thruster, the thrust and the propellant utilization efficiency decreased when using water. The thrust was calculated using efficiency of divergence, the voltage of the screen grid, and the beam current

as

$$F = \sum_j \eta_{\text{div},j} \sqrt{\frac{e}{q_j} \frac{M_j}{M_{\text{prop}}}} \sqrt{\frac{2M_{\text{prop}} V_{\text{SG}}}{e}} I_{\text{b},j}. \quad (24)$$

The beam current was calculated individually for each ion, and 95% of the current of the screen grid was regarded as a beam current. The thrust coefficient was defined as

$$c_T = \sum_j \eta_{\text{div},j} \sqrt{\frac{e}{q_j} \frac{M_j}{M_{\text{prop}}}} \quad (25)$$

to represent the effect of beam divergence, multiply-charged ions, and dissociation. Also, the specific impulse, the propellant utilization efficiency, and ion production cost were defined as

$$I_{\text{sp}} = \frac{F}{\dot{m}_{\text{prop}} g}. \quad (26)$$

$$\eta_U = \frac{M_{\text{prop}} I_{\text{SG}}}{e \dot{m}_{\text{prop}}}. \quad (27)$$

$$C_i = \frac{P_{\text{in}}}{I_{\text{SG}}}. \quad (28)$$

the propellant utilization efficiency should be redefined by including the effect of dissociation for more accurate expression, but here the definition above was used for simplicity especially because of the difficulty in redefining it from the experimental results.

When choosing the operation point with the similar ion production cost, 242 W A⁻¹, in the range of 1.7–1.8 W of the input microwave power in the experiment, the water ion thruster at the mass flow rate of 38.5 ± 1.7 μg s⁻¹ had a thrust of 158 ± 3.4 μN and a propellant utilization efficiency of 3.5% with an assumption that the efficiency of beam divergence was 0.95, which was determined to be consistent to the thrust measurement [40]. The measurement was not enough accuracy to estimate the efficiency and 0.95 was just one example for calculation, thus it should include error from this assumption.

The xenon one at the mass flow rate of 42.7 μg s⁻¹ had a thrust of 433 μN and the efficiency of 23.3% with an assumption that the thrust coefficient was 0.96, which was determined from the result of the on-orbit operation [74]. Considering the application for CubeSat, since it has a strict limit for power and volume, the most important point is whether water is used as a propellant without the significant increase of the ion production cost or not. In that sense, the result showed that it could be achieved and that the possibility of applying the water ion thruster for CubeSat. On the other hand, the lower propellant utilization efficiency directly leads to the lower specific impulse because the specific impulse is almost proportional to the propellant utilization efficiency as shown in equations (24), (26) and (27) while neglecting the mass flow to the neutralizer. It is a major issue for practical application.

Another comparison is the lower limits of the mass flow rate required to sustain the operation in the experiment. During the ion source operation, decreasing the mass flow rate at a given microwave power resulted in plasma extinction at a certain flow rate, whose trends are summarized in figure 12. The trend was similar for both propellants when the microwave power

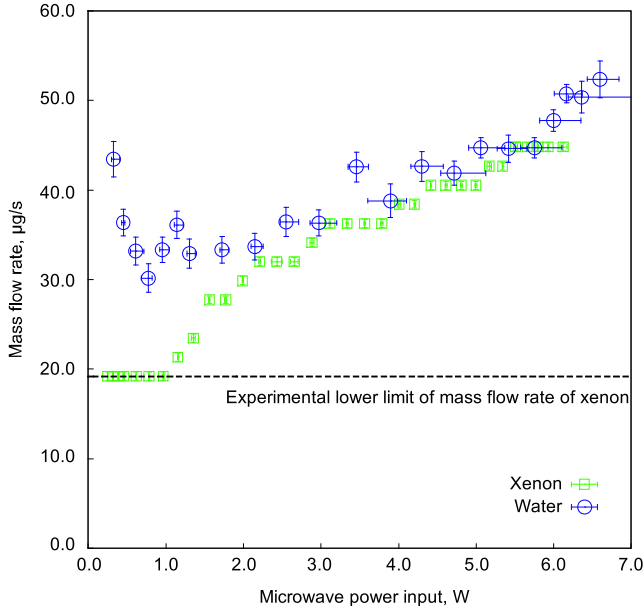


Figure 12. Dependence of the lowest operating mass flow rate on the microwave power.

was higher than 2.0 W, although the water showed slightly higher values than xenon. The extinction would be caused by the decrease of the neutral particle density in which the current increase with the microwave power originated, but it was not reproduced by the model. In a lower power range than 2.0 W, the water curve separated from the xenon one and shows the inverse trend with the microwave power, which also was not reproduced by the model.

5.3. Comparison of the experiment with the model

The global model is useful for comprehending and predicting the behavior of an ion source using water, but in general, the estimated current has a gap from the experiment as shown in figure 13(a). This would be mainly caused by the simplification in the model due to neglecting plasma profiles, magnetization, and the 2D/3D sheath structure. Here, we introduce a parameter which is a ratio of the experimental result to the estimate from the model under every condition defined as:

$$r_{\text{em}}(\dot{m}_{\text{prop}}, P_{\text{abs}}, \text{prop}) = \frac{I_{\text{SG,exp}}(\dot{m}_{\text{prop}}, P_{\text{abs}}, \text{prop})}{I_{\text{SG,mod}}(\dot{m}_{\text{prop}}, P_{\text{abs}}, \text{prop})}. \quad (29)$$

Figure 13(b) shows the dependence of the parameter on the absorbed microwave power with all mass flow rates shown in the result section. The water- and xenon-plasma model have a difference in the dependence on the absorbed microwave power, and both models have a gap from the experiments. They showed the similar trend in the lower power region such as less than 1.0 W, and there was a possibility that it was caused by the inaccuracy of the microwave power in the low power range because it was used in both water and xenon and the error at the lower power range was bigger than that of the higher power range.

The difference between water and xenon should be caused by the physical phenomena which were not included in the

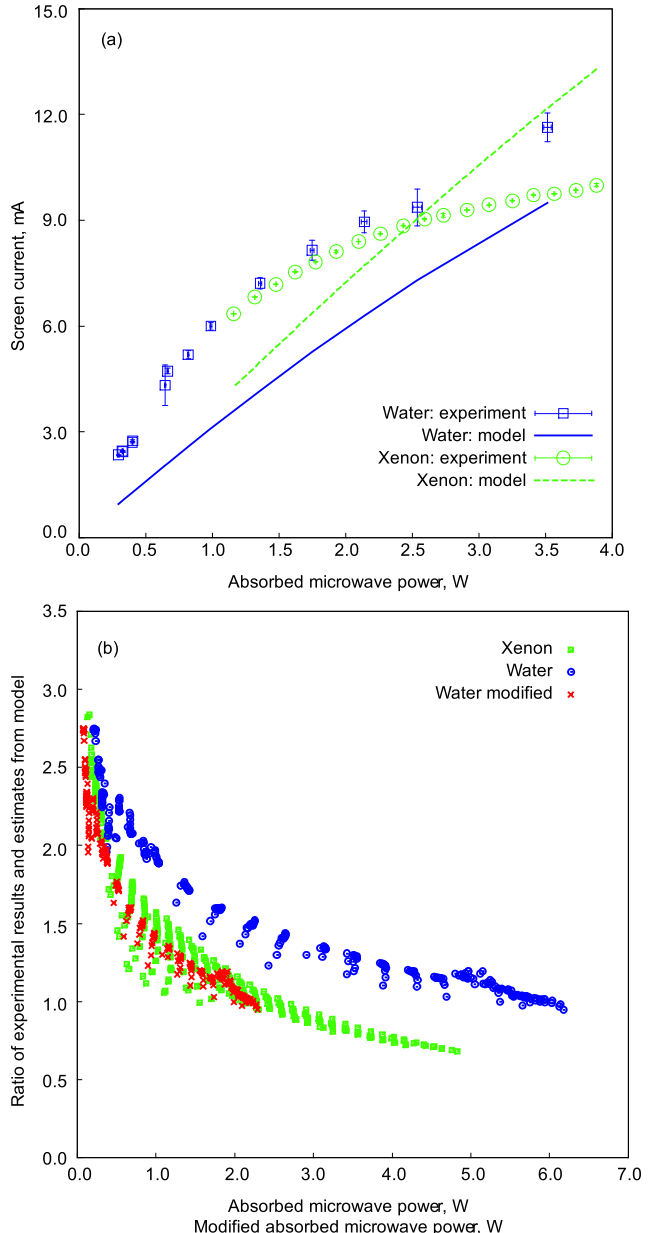


Figure 13. (a) Result of the experiment and in $(40.0 \pm 3.5) \mu\text{g s}^{-1}$ for water and $(40.5 \pm 0.4) \mu\text{g s}^{-1}$ for xenon, and the estimates from the model with $40 \mu\text{g s}^{-1}$ for water and $40.5 \mu\text{g s}^{-1}$ for xenon (b) ratio of the results of the experiments to the estimates from the model with the absorbed microwave power. The data with all mass flow rates used in the experiments are plotted. The horizontal axis of ‘water modified’ plots is modified absorbed microwave power defined in equation (23).

model and also related to the propellant properties. The Bohm velocity, the Child Langmuir limit, and the cyclotron radius of ions are the options. The Bohm velocity characterizes the loss of ions, which affects the rough assumptions related to the loss of ions, for example, on the shape of plasma, which was assumed as a simple cylindrical shape and far from the actual structure. The Child Langmuir limit represents the extraction of the ion beam from the screen grid which was assumed to be as shown by equations (10)–(12). In the view of ion optics, the potential surface which ion was extracted from should be determined to be satisfied the Child Langmuir limit, and the

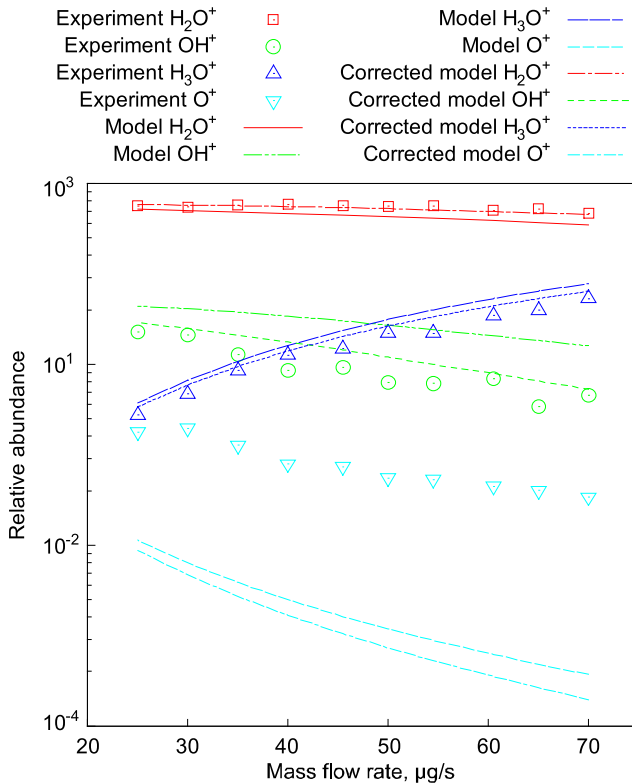


Figure 14. Relative abundance of the ions in the water plasma according to measurement, model and the corrected model. Corrected model included the effect of charge transfer between the ion source and the spectrometer.

sheath was expanded around the screen grid holes [75] but the effect was ignored in the model. The cyclotron radius of ion also affects the extraction in terms of the transportation of the ions to the grid. It is more important in the case of ECR ion thruster because the plasma is strongly trapped by a magnetic field compared with other types of ion thrusters as studied in reference [76]. Especially since the cyclotron radius of water ions is comparable to the scale of the discharge chamber in this case, the effect is not negligible.

Since these physical parameters are in proportion or inverse proportion to the square root of the molecular mass, ‘modified absorbed microwave power’ is introduced to remove these effects on the water ion thruster. It is defined as:

$$P_{\text{modified}} = \sqrt{\frac{M_{\text{H}_2\text{O}}}{M_{\text{Xe}}}} P_{\text{abs},\text{water}}. \quad (30)$$

The points on the water propellant using this modified power as the horizontal axis are also shown in figure 13(b). It would explain the difference between the two propellants, and suggests that the main cause of the difference be the effects as mentioned above such as the Bohm velocity and the Child Langmuir, although there is no physical background for this square root of mass ratio multiplied to the microwave power, not to other parameters such as mass flow rate.

Another validation of the model is the comparison between the measurement and the model concerning the relative abundance of the ions as shown in figure 14. The trend of the mass flow rate was reproduced well in the model, especially

for H_2O^+ , OH^+ , and H_3O^+ . The estimates on O^+ was much lower in the experiment. It would be caused by neglecting the neutral O which could be ionized to O^+ . Also, the vacuum chamber pressure affected the result because it increases the charge-exchanged ions between the ion source and the spectrometer. For instance, the mean free path of H_2O^+ at the highest mass flow was about 12 cm, and it is a similar amount of the length between the ion source and the spectrometer: 7 cm. The charge-exchanged ions affected the measured relative abundance, and it was roughly estimated with the assumption that all of the generated ions between the ion source and the spectrometer were measured by the spectrometer. The modified model results are also shown in figure 14. The trend does not change, and the part of the difference between the model and the experiment would be explained this effect, especially in the case of OH^+ . The relative abundance given by the model would have enough accuracy for order estimation and the model suggested that H^+ and H_2^+ , which could not be measured in the experiments, were present only in small amounts to not affect the thrust.

5.4. Discussion about performance decreasing based on the model

The comparison based on the model suggests that the increasing loss of the heavy particle because of the lighter molecule and the lower ionization cross-section should be a reason for the decrease in performance. Figure 15(a) compares the major parameters in the water- and xenon-plasma models. Under the same mass flow rate, the neutral particle density of water was only three times higher than that of xenon despite its volume flow rate was more than seven times larger. It was because the gas conductance of accelerating grids shown in equation (9), which mainly determined the density, became about 37% of xenon due to the difference of the mass of the molecule. This claimed that one cause of the performance drop was due to a lighter molecule of water. Furthermore, the electron density was about one-fifth of xenon even though the neutral particle density was higher. It would be caused by the increase of the ion loss by the higher electron temperature and plasma potential due to the lower ionization cross-section and the higher Bohm velocity. As a result, the ion production cost increased and the propellant utilization efficiency, which affected all the negative effects mentioned above, decreased about one-tenth of xenon. To compare them at the same ion production cost, the result from the water-plasma model at a mass flow rate of $58.5 \mu\text{g s}^{-1}$ is also shown. Although the electron temperature and the plasma potential decreased owing to higher neutral particle density, the propellant utilization efficiency got worse.

Figure 15(b) also shows the detail of energy loss in these three conditions. The loss in ionization was comparable in all cases, around 20% of absorbed power was used for ionization. The loss in electronic excitation in water plasma was much smaller than that of xenon at the same mass flow rate, and the other losses increased. The loss in dissociation had a significant value, which was around 10% of absorbed power, and it shows the importance of dissociation in weakly ionized low-pressure water plasma such as this case. The other unique losses of water were vibrational and rotational

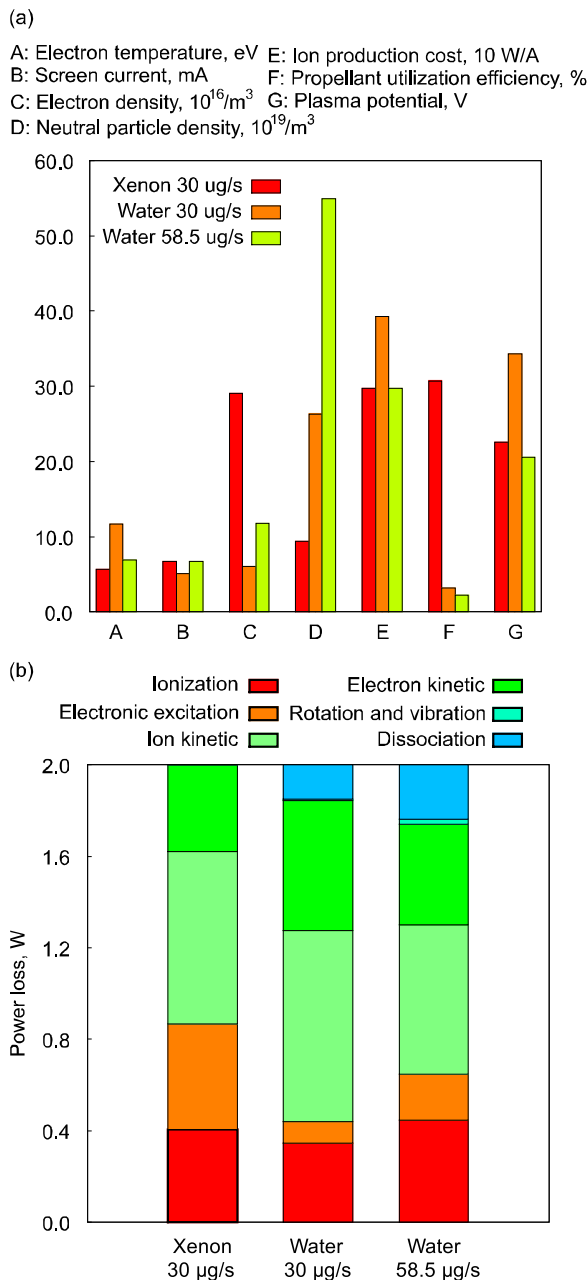


Figure 15. (a) Major parameters based on the model at the absorbed microwave power of 2.0 W and the mass flow rate of $30 \mu\text{g s}^{-1}$ for water and xenon, and $58.5 \mu\text{g s}^{-1}$ for water. $58.5 \mu\text{g s}^{-1}$ was chosen as the screen current became the same as that of the xenon one. (b) Values of the power loss terms described in equation (1) under the three conditions. The elastic scattering was not shown because the value was less than 0.05% of the total power loss.

excitation. These were less than 30 mW, 1.5% of absorbed power, and had a limited effect on the plasma.

6. Conclusion

A microwave-discharge miniature ion thruster using water and xenon as propellants was examined by a model and experiments. A global model for the ion source was built to estimate and compare the performances. The experiments were conducted by measuring the beam current under

various conditions and the relative abundance of ions by a quadrupole mass spectrometer. At a microwave power input of 0.25–6.0 W, the highest beam currents were about 12 mA for xenon and 18 mA for water. In the comparison between the model and the experimental results, the two differences, the difference between water and xenon and the difference from the experimental result in both cases, were discussed. The Bohm velocity, the Child Langmuir limit, and the cyclotron radius of ions were candidates that have the effect which departs from the model. The difference from the experimental results would be caused by the assumptions on the model. The measured relative abundance matched the model in the order and the trend, and it was shown that the small fractions from dissociative reactions did not affect the thrust very much. By the comparison based on the model, the power used for ionization did not differ from that of xenon and the loss in electronic excitation was smaller than that of xenon. By contrast, the loss in dissociation, which is unique to water, was significant.

A performance decrease in the propellant utilization efficiency and the specific impulse cannot be avoided when using water as a propellant in an ion thruster if the same design or concept is followed as when using xenon because of the limitation shown in the model, especially the lighter molecule of water and the lower ionization cross-section. In the view of an application for CubeSat, the fact that the ion production cost did not increase is important because it meant the required power did not increase. It showed the minimum capability of water ion thruster for CubeSat application because water itself has a big advantage when used as a propellant for CubeSat propulsion such as safety, low cost, non-pressurized system, and human-friendliness. As further research, increasing the propellant utilization efficiency of the water ion thruster is a more important and promising issue because the capability was shown, and it requires additional modifications of ion source to exceed the model of the current design.

Acknowledgments

This work was supported by JSPS KAKENHI Grant Number JP16H06370.

ORCID iDs

Yuichi Nakagawa <https://orcid.org/0000-0001-6349-4018>
 Hiroyuki Koizumi <https://orcid.org/0000-0003-0120-1958>
 Kimiya Komurasaki <https://orcid.org/0000-0003-1695-3255>

References

- [1] Lev D, Myers R M, Lemmer K M, Kolbeck J, Koizumi H and Polzin K 2019 *Acta Astronaut.* **159** 213–27
- [2] Brophy J, Garner C, Nakazono B, Marcucci M, Henry M and Noon D 2003 The ion propulsion system for Dawn AIAA 2003-4542
- [3] Kuninaka H, Nishiyama K, Funaki I, Yamada T, Shimizu Y and Kawaguchi J 2007 *J. Propul. Power* **23** 544–51
- [4] Goebel D, Lavin M M, Bond T and King A 2002 Performance of XIPS electric propulsion in on-orbit station keeping of the Boeing 702 spacecraft AIAA 2002-4348

- [5] Linnell J A and Gallimore A D 2006 *J. Propul. Power* **22** 1402–12
- [6] Kieckhafer A and King L B 2007 *J. Propul. Power* **23** 21–6
- [7] Szabo J, Pote B, Paintal S, Robin M, Hillier A, Branan R D and Huffmann R E 2012 *J. Propul. Power* **28** 848–57
- [8] Shabshelowitz A, Gallimore A D and Peterson P Y 2014 *J. Propul. Power* **30** 664–71
- [9] Gurciullo A, Lucca Fabris A and Knoll A 2017 *IEEE Trans. Plasma Sci.* **45** 2472–80
- [10] Holste K, Gärtner W, Zschätzsch D, Scharmann S, Köhler P, Dietz P and Klar P J 2018 *Eur. Phys. J. D* **72** 9
- [11] Dietz P, Gärtner W, Koch Q, Köhler P E, Teng Y, Schreiner P R, Holste K and Klar P J 2019 *Plasma Sources Sci. Technol.* **28** 084001
- [12] Charles C, Boswell R W, Laine R and MacLellan P 2008 *J. Phys. D: Appl. Phys.* **41** 175213
- [13] Bathgate S N, Bilek M M M and Mckenzie D R 2017 *Plasma Sci. Technol.* **19** 083001
- [14] Krejci D and Lozano P 2018 *Proc. IEEE* **106** 362
- [15] Poghosyan A and Golkar A 2017 *Prog. Aerosp. Sci.* **88** 59–83
- [16] Pottinger S J, Krejci D and Scharlemann C A 2011 *Acta Astronaut.* **68** 1996–2004
- [17] Rezaeih A and Schönher T 2014 *J. Propul. Power* **30** 253–64
- [18] Ciaralli S, Coletti M and Gabriel S B 2016 *Acta Astronaut.* **121** 314–22
- [19] Woodruff C, King D, Burton R, Bowman J and Carroll D 2019 Development of a fiber-fed pulsed plasma thruster for small satellites *Proc. Small Satellite Conf.* 2019
- [20] Krejci D, Mier-Hicks F, Thomas R, Haag T and Lozano P 2017 *J. Spacecr. Rockets* **54** 447–58
- [21] Reissner A, Buldrini N, Seifert B, Hörbe T and Plesescu F 2016 The IFM nano thruster—introducing very high Δv capabilities for nanosats and CubeSats *AIAA 2016-5044*
- [22] Nakagawa Y, Koizumi H, Kawahara H and Komurasaki K 2019 *Acta Astronaut.* **157** 294–9
- [23] Koizumi H, Asakawa J, Nakagawa Y, Nishii K, Takao Y, Nakano M and Funase R 2019 *J. Spacecr. Rockets* **56** 1400–8
- [24] Martinez J M, Rafalskyi D and Aanesland A 2019 *Proc. 36th Int. Electric Propulsion Conf. IEPC-2019-811*
- [25] Hraby P, Demmons N, Courtney D, Tsay M, Szabo J and Hraby V 2019 *Proc. 36th Int. Electric Propulsion Conf. IEPC-2019-926*
- [26] Bosanac N, Cox A D, Howell K C and Folta D C 2018 *Acta Astronaut.* **144** 283–96
- [27] Tsay M and Courtney D 2019 All-electric CubeSat propulsion technologies for versatile mission applications *2019 Proc. 32nd Int. Symp. Space Technology and Science*
- [28] Guerrieri D C, Silva M A C, Cervone A and Gill E 2017 *J. Heat Transfer* **139** 102001
- [29] Yaginuma K et al 2020 *Trans. Japan Soc. Aeronaut. Space Sci.* **18** 141–8
- [30] Cervone A, Zandbergen B, Guerrieri D C, De Athayde Costa e Silva M, Krusharev I and van Zeijl H 2017 *CEAS Space J.* **9** 111–25
- [31] Asakawa J, Koizumi H, Nishii K, Takeda N, Murohara M, Funase R and Komurasaki K 2018 *Trans. Japan Soc. Aeronaut. Space Sci., Aero. Technol. Japan* **16** 427–31
- [32] Nishii K et al 2020 *Trans. Japan Soc. Aeronaut. Space Sci.* **63** 141–50
- [33] Scharlemann C A and York T M 2003 Pulsed plasma thruster using water propellant, part I: design and investigation of thrust behavior *AIAA 2003-5022*
- [34] Koizumi H, Kakami A, Furuta Y, Komurasaki K and Arakawa Y 2003 Liquid propellant pulsed plasma thruster *Proc. 28th Int. Electric Propulsion Conf. IEPC-03-087*
- [35] Kuninaka H and Satori S 1998 *J. Propul. Power* **14** 1022
- [36] Koizumi H and Kuninaka H 2009 *Trans. Japan Soc. Aeronaut. Space Sci., Aero. Technol. Japan* **7 Pb_89**–94
- [37] Koizumi H and Kuninaka H 2010 *J. Propul. Power* **26** 601
- [38] Koizumi H et al 2016 *Trans. Japan Soc. Aeronaut. Space Sci., Aero. Technol. Japan* **14 Pb_13**–22
- [39] Koizumi H, Komurasaki K, Aoyama J and Yamaguchi K 2018 *J. Propul. Power* **34** 960–8
- [40] Nakagawa Y, Tomita D, Koizumi H and Komurasaki K 2018 *Trans. Japan Soc. Aeronaut. Space Sci., Aero. Technol. Japan* **16** 152
- [41] Nakamura K, Koizumi H, Nakano M and Takao Y 2019 *Phys. Plasmas* **26** 043508
- [42] Lichtenberg A J, Vahedi V, Lieberman M A and Rognlien T 1994 *J. Appl. Phys.* **75** 2339–47
- [43] Meyyappan R and Govindan T R 1995 *IEEE Trans. Plasma Sci.* **23** 623–7
- [44] Wu H-M, Graves D B and Porteous R K 1995 *Plasma Sources Sci. Technol.* **4** 22–30
- [45] Lee C and Lieberman M A 1995 *J. Vac. Sci. Technol. A* **13** 368–80
- [46] Brophy J R 1984 Ion thruster performance model NASA CR-174810 *PhD Thesis* Colorado State University, Fort Collins
- [47] Goebel D M, Wirz R E and Katz I 2007 *J. Propul. Power* **23** 1055–67
- [48] Grondein P, Lafleur T, Chabert P and Aanesland A 2016 *Phys. Plasmas* **23** 033514
- [49] Petro E M and Sedwick R J 2017 *J. Propul. Power* **33** 1410–7
- [50] Itikawa Y and Mason N 2005 *Phys. Rep.* **414** 1–22
- [51] Chuqian A, Hall R I and Trajmar S 1975 *J. Chem. Phys.* **63** 892–8
- [52] Gil T J, Rescigno T N, McCurdy C W and Lengsfeld B H 1994 *Phys. Rev. A* **49** 2642–50
- [53] Matsui M, Hoshino M, Kato H, Silva F F, Vieira P L and Tanaka H 2016 *Eur. Phys. J. D* **70** 77
- [54] Kim Y K 2001 *Phys. Rev. A* **64** 032713
- [55] Durante N, Lamanna U T, Arrighini G P and Guidotti C 1995 *Theor. Chim. Acta* **90** 115–34
- [56] Thorn P A, Brunger M J, Kato H, Hoshino M and Tanaka H 2007 *J. Phys. B: At. Mol. Opt. Phys.* **40** 697–708
- [57] Avtaeva S V, General A A and Kel'man V A 2010 *J. Phys. D: Appl. Phys.* **43** 315201
- [58] Mathur D and Badrinath C 1987 *Phys. Rev. A* **35** 1033–42
- [59] Rejoub R, Lindsay B G and Stebbings R F 2002 *Phys. Rev. A* **65** 042713
- [60] Filipovic D, Marinkovic B, Pejcev V and Vuskovic L 1998 *Phys. Rev. A* **37** 356–64
- [61] Hayashi M 1983 *J. Phys. D: Appl. Phys.* **16** 581–9
- [62] Miller J S, Pullins S H, Levandier D J, Chiu Y-H and Dressler R A 2002 *J. Appl. Phys.* **91** 984–91
- [63] Lindsay B G and Mangan M A 2003 *Photon and Electron Interactions with Atoms, Molecules and Ions, Landolt-Börnstein* (Berlin: Springer)
- [64] Thorn P A et al 2007 *J. Chem. Phys.* **126** 064306
- [65] Santeler D J 1986 *J. Vac. Sci. Technol. A* **4** 338–43
- [66] Dawson P H 1976 *Quadrupole Mass Spectrometry and its Applications* (Amsterdam: Elsevier)
- [67] Meija J et al 2016 *Pure Appl. Chem.* **88** 293–306
- [68] Hiramoto K, Nakagawa Y, Koizumi H and Takao Y 2017 *Phys. Plasmas* **24** 064504
- [69] Nakamura K, Nakagawa Y, Koizumi H and Takao Y 2018 *Trans. Japan Soc. Aeronaut. Space Sci.* **61** 152–9
- [70] Nakano M, Nakamura K, Nakagawa Y, Tomita D, Takao Y and Koizumi H 2018 *Phys. Plasmas* **25** 013524
- [71] Lagarde T, Arnal Y, Lacoste A and Pelletier J 2001 *Plasma Sources Sci. Technol.* **10** 181–90
- [72] Toader E I 2004 *Plasma Sources Sci. Technol.* **13** 646
- [73] Singh S B, Chand N and Patil D S 2009 *Vacuum* **83** 372–7
- [74] Koizumi H, Kawahara H, Yaginuma K, Asakawa J, Funase R and Komurasaki K 2015 *Proc. 34th Int. Electric Propulsion Conf. IEPC-2015-276*
- [75] Goebel D M and Katz I 2008 *Fundamentals of Electric Propulsion: Ion and Hall Thrusters* (New York: Wiley)
- [76] Tani Y, Tsukizaki R, Koda D, Nishiyama K and Kuninaka H 2019 *Acta Astronaut.* **157** 425–34